Journal of Manufacturing Processes 36 (2018) 281–292

Contents lists available at ScienceDirect

Journal of Manufacturing Processes

journal homepage: www.elsevier.com/locate/manpro

Investigation on the microstructure—mechanical property correlation in dissimilar steel welds of stainless steel SS 304 and medium carbon steel EN 8

Dilip Kumar Singh[a], Gadadhar Sahoo[b], Ritwik Basu[a,*], Vikram Sharma[c], M.A. Mohtadi-Bonab[d]

[a] Department of Mechanical and Manufacturing Engineering, Manipal Institute of Technology, Manipal Academy of Higher Education (MAHE), Manipal, 576104, Karnataka, India
[b] R&D Center for Iron and Steel (RDCIS), Steel Authority of India Ltd., Ranchi, 834002, Jharkhand, India
[c] Research and Development Division, Tata Steel Ltd., Jamshedpur, 831001, Jharkhand, India
[d] Department of Mechanical Engineering, University of Bonab, Bonab, Iran

ARTICLE INFO

Keywords:
Dissimilar welding
Tungsten inert gas (TIG) welding
Electron backscattered diffraction (EBSD)
In-grain misorientation
Low angle grain boundary (LAGB)
Stored energy

ABSTRACT

Stainless steel grade SS 304 and medium carbon steel EN 8 were welded with various combinations of weld parameters using tungsten inert gas (TIG) welding process. Significant differences in weld and interface microstructures were achieved under different weld process variables (current, voltage and speed). Microstructures of the weld region varied from large grains of γ-austenite to fine grain distribution of δ-ferrite and γ-austenite grains. Further to that, the phase boundaries between γ and δ phases showed presence of two dominant phase boundary relationships (PBR), 44°⟨104⟩ and 44°⟨114⟩. The weld metal (WM)-base metal (BM) interfaces also showed differences in the fusion zone (FZ) and heat affected zone (HAZ). Fusion zone at the interface of medium carbon steel and weld metal were characterized by presence of fine grains of ferrite which were identified as relatively strain free grains. These differences in microstructures were mainly due to the differences in heat inputs and solidification rates of the weld metal. Differences were also observed in the grain boundary fractions and local in-grain misorientation between different microstructures. The tensile strength of these welded joints were found to be clear functions of low angle grain boundary (LAGB) fractions, while impact energy was seen to be a function of austenite in-grain misorientation and δ-ferrite percentage. The pattern of fracture under tensile deformation displayed both mixed mode and ductile fracture. Differences in the fractured surfaces were seen in the distribution, size and shapes of dimples and microvoids. The present investigation attempts to address the pattern of microstructure development and the related mechanical behavior in dissimilar welded joints through a systematic approach.

1. Introduction

The subject of joining the dissimilar metal involves a wide range of materials and manufacturing processes. In many engineering applications, the combined presence of stainless steel and carbon steel is necessary. Thus, for such applications, the fabrication of components and assemblies requires dissimilar welds of high quality [1,2]. Challenges related to the welding of dissimilar steel grades include the manufacturing of pressure vessels, boilers, heat exchangers used in the power generation industry, petrochemical plants, etc. [3,4]. Austenitic stainless steel pipes are widely used to transport high temperature-high pressure steam in power plants. However, below certain temperature and pressure, medium carbon steels can also meet the requirements. As a result, the transition from stainless steel to other grades of steel is economical under certain conditions. Nevertheless, dissimilar welding of steels results in many metallurgical difficulties, such as solidification cracks, hydrogen cracks and formation of brittle phases, which can cause component failure before the expected service life [3–6].

Both solid state [7–10] and fusion welding [11–16] processes for joining dissimilar metals are evident in literature. Among the fusion welding techniques, tungsten inert gas (TIG) welding is mostly adopted for applications which require a high level of weld quality or precision [11,12,17–20]. This technique uses an arc between a non-consumable tungsten electrode and the dissimilar metal parts to be welded under a shielding gas environment. However, the joining of stainless steel to medium carbon steels by fusion welding has a disadvantage of forming harmful carbides in the weld metal. This results in decarburization and grain growth occurring in the heat affected zone (HAZ) of carbon steel, which deteriorate the mechanical properties [21]. At the same time, carbide formation in the weld metal will substantially increase the

* Corresponding author.
E-mail address: basu.ritwik@gmail.com (R. Basu).

https://doi.org/10.1016/j.jmapro.2018.10.018
Received 13 August 2018; Received in revised form 30 September 2018; Accepted 19 October 2018

hardness of the weld and the possibility of cracks in this region as well. Differences in coefficient of thermal expansion and thermal conductivity may also be problematic [22–24]. Stainless steel will have the tendency to expand and contract due to the high heat input during welding. On the other hand, carbon steel which is a good conductor of heat, cools faster and shrinks rapidly as the joint cools. These differences increase the residual stresses at the junction causing warping or misalignment of the weld component. These stresses caused by thermal expansion and contraction can exceed the strength of one or the other material leading to crack formation. The properties and failure behavior of the weld joints can be largely altered by tailoring the microstructure. This paper provides an insight into the microstructure—mechanical property relationships in fusion weld joints of two different grades of steels, stainless steel SS 304 and medium carbon steel EN 8 prepared through TIG welding processes.

There are numerous studies on the microstructure development in dissimilar welds of steels [25–29], however no comprehensive quantitative mechanism for relating microstructure to the mechanical properties has been given. A detailed microstructural analysis on the grain boundary nature, misorientation in the microstructures, phase boundary relationship on the mechanical behavior of the weld specimens is investigated in this study. Five different sample conditions were prepared under different process variables. The microstructural development of the interfaces and weld region has been studied through optical microscopy and electron backscattered diffraction (EBSD) techniques. A correlation is established between the strength of the welds to the low-angle grain boundary (LAGB) fractions and the stored energy of the LAGBs. The mode of failure during tensile loading and impact testing has also been studied in the present investigation. The motivation of the study was to establish a consolidated understanding on the microstructural developments and its correlation to the related changes in the mechanical properties.

2. Experimental methods

The two different steel grades chosen for the present investigation were stainless steel SS 304 and medium carbon steel EN 8 in the rolled and annealed states. Rectangular plates of both grades were sectioned into 60 mm (length) × 30 mm (width) × 4 mm (thickness) dimensions. Both the base materials were thoroughly cleaned to remove contamination like rust, dust, oil and moisture to avoid welding defects that may arise due to any contamination of the base metal. These two grades of steels were laterally butt-welded using TIG welding under full penetration on the cut sections by applying single electric arc discharge on one face with 309 L as the filler material. 309 L is the preferred filler material in joining austenitic stainless steel to carbon steels to prevent the formation of martensite. This also preserves the residual amounts of ferrite, which prevent hot cracking tendencies, even under severe conditions. Chemical composition of the two grades of steel used for the study is presented in Table 1. The welding current, voltage and welding speed were varied to obtain different heat inputs. The heat inputs were calculated from the empirical relation in Eq. (1).

$$H_i = A^*V^*\frac{0.06}{s} \quad (1)$$

Where,

Table 1
Composition of alloying elements in percentages of the as-received base material and filler material used in the present study.

	Grade	C	Si	Mn	S	P	Cr	Cu	Mo	Ni
Base Material	EN8	0.38	0.25	0.7	0.04	0.04				
Base Material	SS 304	0.07	0.75	2.0	0.03	0.04	19			10
Filler Material	309 L	0.03	0.45	1.5	0.03	0.03	24	0.70	0.70	12

H_i – heat input required in kJ/mm
A – welding current A in Amps
V – arc voltage in volts
s – welding speed in mm/min

Five different samples, generically termed as A, B, C, D and E were prepared under different weld process variables. The weld parameters are summarized in Table 2.

Tensile specimens with dimension 120 mm (length) × 20 mm (width) × 3.5 mm (thickness) were machined from the weld plates as per the ASTM E8M standard. Fig. 1a presents the schematic of the tensile specimen geometry. The specimens were cut so that the weld was located in the middle of the specimen gauge. After machining, the gauge area was polished with SiC paper and then rinsed ultrasonically in an acetone bath. The tensile tests were performed in a 50 kN Universal Testing Machine ITW BISS. The deformation was carried out at 20 kN/min till the complete failure of the specimens.

All the welded specimens were subjected to the Charpy impact test. The V-notches with (10 × 10) mm^2 section and 45° notch angle were prepared at the weld centers of all the specimens. The V notch was created in a way such that the notch plane remained perpendicular to the long transverse direction.

For microstructural analysis, specimens were mechanically polished through standard metallographic techniques followed by polishing in

Table 2
Welding parameters used in the present study.

Sample	Voltage (V)	Current (A)	Speed (mm s^{-1})	Heat Input (kJ mm^{-1})
A	13.6	100	2.67	0.5093
B	13.2	95	2.27	0.5524
C	17.5	90	3.55	0.4436
D	12.6	100	3.55	0.3549
E	12.6	100	4.57	0.2757

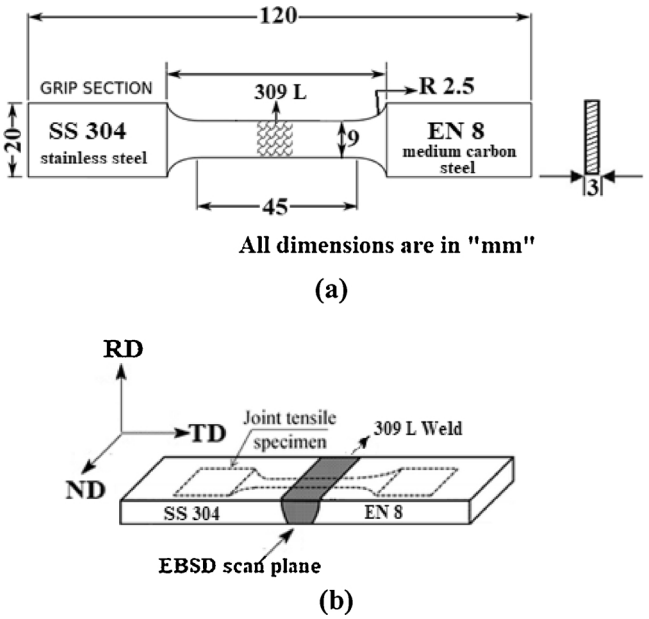

Fig. 1. (a) Geometry of the tensile specimen used in the present study. Samples were prepared according to ASTM E8M standards. Shaded areas indicate the approximate location of the weld zone. (b) Scheme of the welded material together with the orientation of the tensile specimen. The materials at different regions of the welded specimens are indicated in the schematic. The reference directions (RD, roll direction, TD, transverse direction, ND, normal direction) with respect to the sample system are shown.

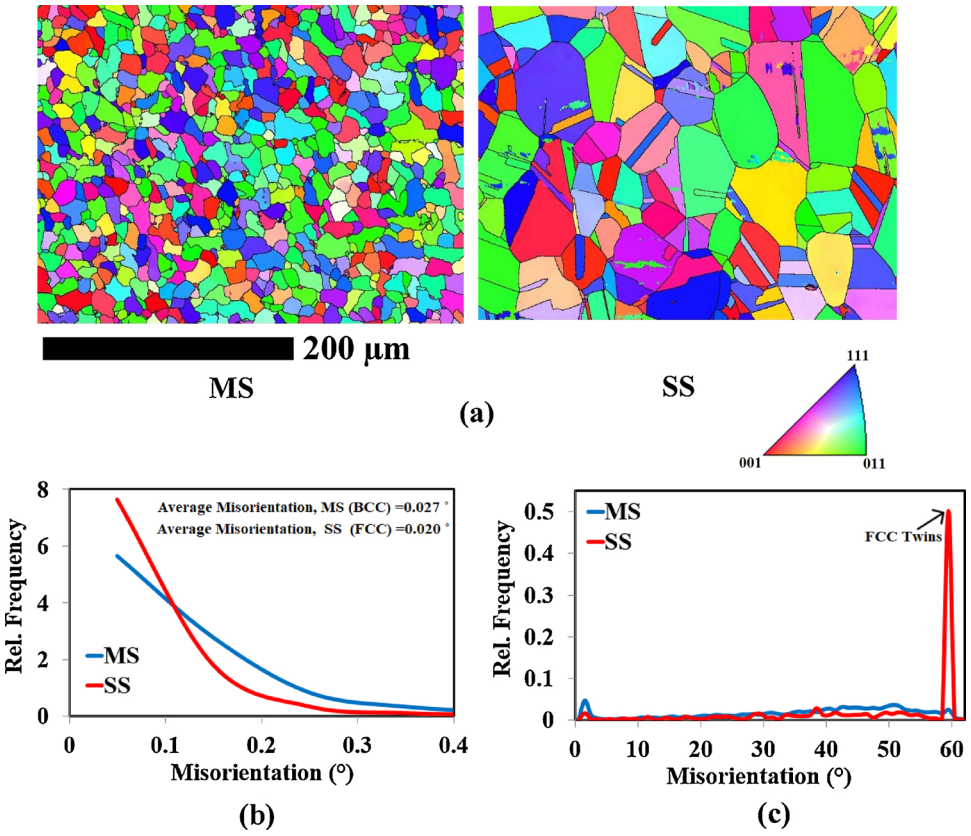

Fig. 2. (a) EBSD (electron backscattered diffraction) measured inverse pole figure (IPF) map of medium carbon steel (MS)-bcc and stainless steel (SS)-fcc. The colors in the IPF map represent the crystal directions parallel to the normal direction (ND) of the sample reference system. (b) Local misorientation distribution plot for the two steel grades. The inset shows the average misorientation values. (c) Grain boundary distribution plot. The increased frequency at around 60 ° for the SS is due to the large presence of annealing twins. (Color figure online).

diamond suspension medium. For optical microscopy, the samples were treated with a suitable chemical etchant (1 part of HNO_3, 1 part of HCl and 1 part of distilled H_2O) by volume to bring out the microstructure details. For electron backscattered diffraction (EBSD) studies, the samples were further polished for 20 min. in colloidal silica medium to create a strain free surface. Samples were analyzed for EBSD measurements in a Zeiss Supra 25 field emission gun scanning electron microscope (FEG–SEM) operated at an acceleration voltage of 20 keV. An Oxford Instruments Nordlys 2 EBSD detector coupled with the SEM was used for performing the measurements. A typical scan step size of 0.5 µm was chosen for all samples. The fractography analysis were carried out in a Zeiss EVO 18 special edition SEM operated at 18 keV.

The acquired raw EBSD data were processed for further analysis using the Oxford Instruments Channel 5 post processing software. Grain boundaries (GBs) were identified as continuously bounded misorientation > 5°. GBs greater than 15° were taken as high-angle grain boundaries (HAGBs) while boundary misorientations between 2 and 5° were categorized as low-angle boundaries (LAGBs). Between 5 and 15° misoientation, the GBs were defined as medium-angle boundaries (MAGBs). Local in-grain misorientations were measured for all samples. The measurement considers average point-to-point misorientation inside an identified grain [30]. The stored energy per unit volume due to a grain boundary dislocation (E_b) was obtained from the Read-Shockley equation [31] by multiplying the average energy per unit boundary area ($\bar{\gamma}$) to the area per unit volume:

$$E_b = S_V.\ \bar{\gamma} = \frac{3\bar{\gamma}}{d_{ECD}} \tag{2}$$

where, d_{ECD} is the average grain size measured from equivalent circle diameter considering all misorientations between $5^\circ < \theta < 62.8^\circ$.

Thus, the average boundary energy is calculated by considering all the boundary misorientations between $5^\circ < \theta < 62.8^\circ$ via summation.

$$\bar{\gamma} = \sum_{5}^{62.8} \gamma(\theta).\ f(\theta) \tag{3}$$

where,

$$\gamma(\theta) = \gamma_m\left(\frac{\theta}{\theta_m}\right)\left[1 - ln\left(\frac{\theta}{\theta_m}\right)\right];\ \theta \le \theta_m \tag{4}$$

and,

$$\gamma(\theta) = \gamma_m;\ \theta \ge \theta_m \tag{5}$$

Here $\gamma_m = 0.80\ Jm^{-2}$ [32] is the energy per unit area of a HAGB, θ is the boundary misorientation and $\theta_m = 15^\circ$ is the misorientation angle above which the energy per unit area is independent of misorientation angle. $f(\theta)$ represents the boundary fraction for a given misorientation.

3. Results and discussions

In the present investigation, the weld cross section area was examined for all samples for both optical and EBSD studies. The normal direction (ND), rolling direction (RD) and transverse direction (TD) is presented in Fig. 1b relative to the sample. Fig. 2(a, b) presents the base metal microstructures of medium carbon steel EN8 (MS) and stainless steel SS 304 (SS), represented through EBSD measured inverse pole figure (IPF) maps. The colors in the maps represent the various z-normal directions (NDs) relative to the sample reference. For interpretation of colors, readers are advised to refer the standard colored stereographic triangle. Differences in the two microstructures were brought out through in-grain misorientation distribution and their average values, as shown in Fig. 2c. The grain boundary distribution in Fig. 2c clearly shows large presence of fcc twins, 60° about a ⟨111⟩ axis in SS.

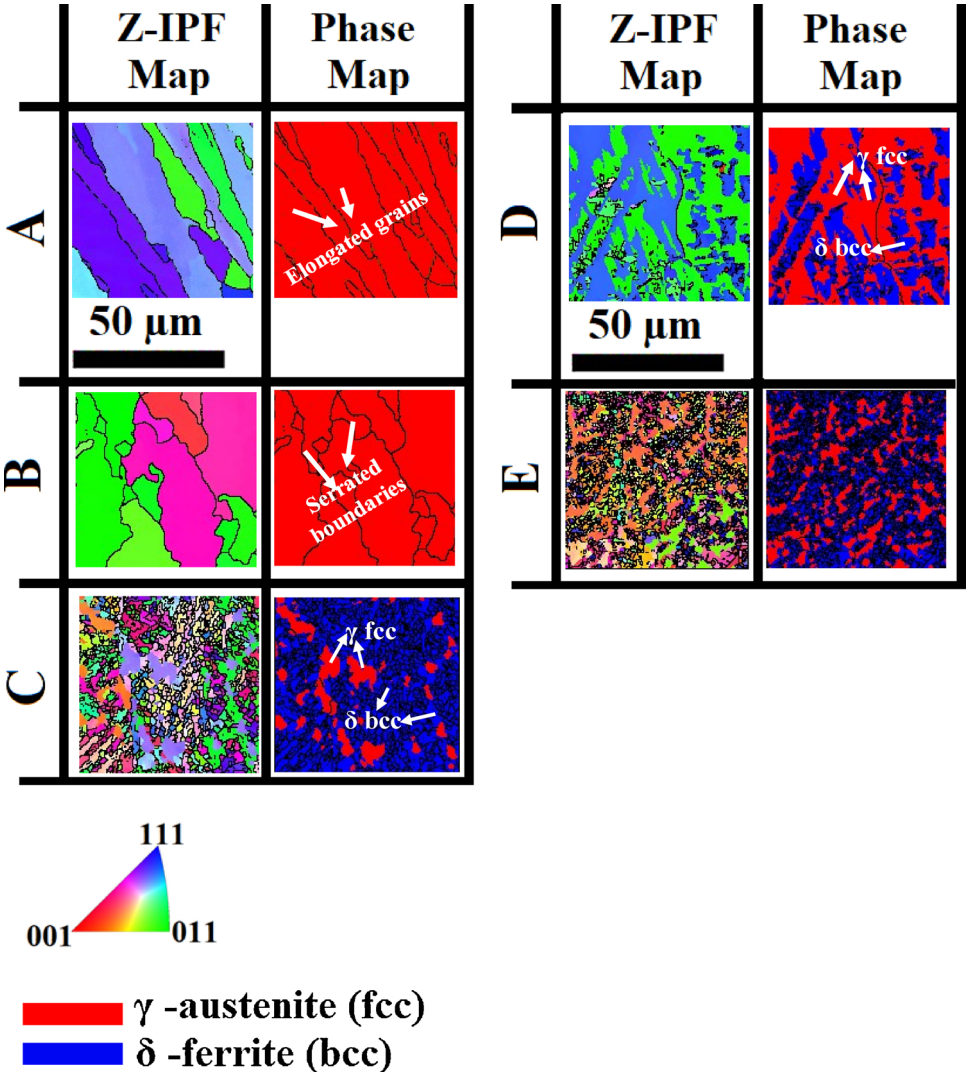

Fig. 3. Microstructural development in the weld metal (WM) region for all specimens under different heat inputs seen through IPF and phase maps. Microstructural features included elongated lamellar grains, serrated grain boundaries and mixed phase distribution of bcc (δ) and fcc (γ). Weld microstructures of Samples C, D and E exhibits a mixed phase distribution of δ bcc and γ fcc phases illustrated through IPF and phase maps. These differences were brought out mainly due to differences in the heat inputs during welding. (Color figure online).

3.1. Microstructural development in the weld metal region

Fig. 3 summarizes the microstructural development of the weld metal region. The IPF and phase maps of the weld metal are included for reference. The microstructures presents elongated lamellar grains, serrated grain boundaries and distribution of bcc and fcc phases. Careful examination of the microstructure of the welds in samples C, D and E reveals a mixed phase distribution of austenite and ferrite. The presence of ferrite in samples A and B was practically insignificant. It is well established that the ferrite that forms during cooling of stainless steel weld or casting is the retained ferrite or δ-ferrite with complex morphology. The factors that control the δ-ferrite formation during solidification, are the variations in composition of stainless steel, presence of alloying elements, and non-equilibrium cooling of weld [33,34].

In the present investigation, it appears from the microstructure of sample D that, the first phase to solidify was austenite (primary phase) and δ-ferrite solidification occurred from the remaining melt, see Fig. 3. It is speculated that during the solidification of primary γ austenite, Cr was rejected into the residual melt which initiated the formation of δ-ferrite [35].

The solidification in the sample E-weld was possibly the opposite type. It started with the solidification of δ-ferrite and γ austenite solidified from remaining melt as seen in Fig. 3. In this situation, formation of δ-ferrite during solidification resulted in rejection of nickel into the melt. When the desired Ni concentration was reached, nucleation of the γ-austenite phase occurred, which continued to grow. It can also be seen in the sample E, there are no interconnections between the γ/γ boundaries and each grain is surrounded by finely distributed δ-ferrite grains. In this situation, the δ-ferrite would have grown in the neighboring austenite grains inhibiting boundary migration and also retarded the growth of austenite grains.

The microstructure of sample C suggests a two-step process- solidification of δ-ferrite directly from the melt, and precipitation of austenite from the solid ferrite under slower cooling rate. It must be mentioned that, the presence of δ-ferrite along γ austenite boundaries exerts a pinning pressure on the γ grain boundaries, which counteracts the driving force for migration of boundaries [36]. Thus, larger the amount of δ-ferrite precipitation, the smaller the size of the austenite grains.

Optical examination was also carried to confirm the findings of EBSD. The optical micrographs in Fig. 4(a–e) shows the morphology and distribution of δ-ferrite in samples A, B, C, D and E. The phase fraction of δ-ferrite, estimated using an image analyzer (ImageJ) program, is included for reference in all the micrographs. All these images had a skeletal ferrite distribution. Though nothing concrete on the growth mechanism of ferrite can be inferred from the optical studies,

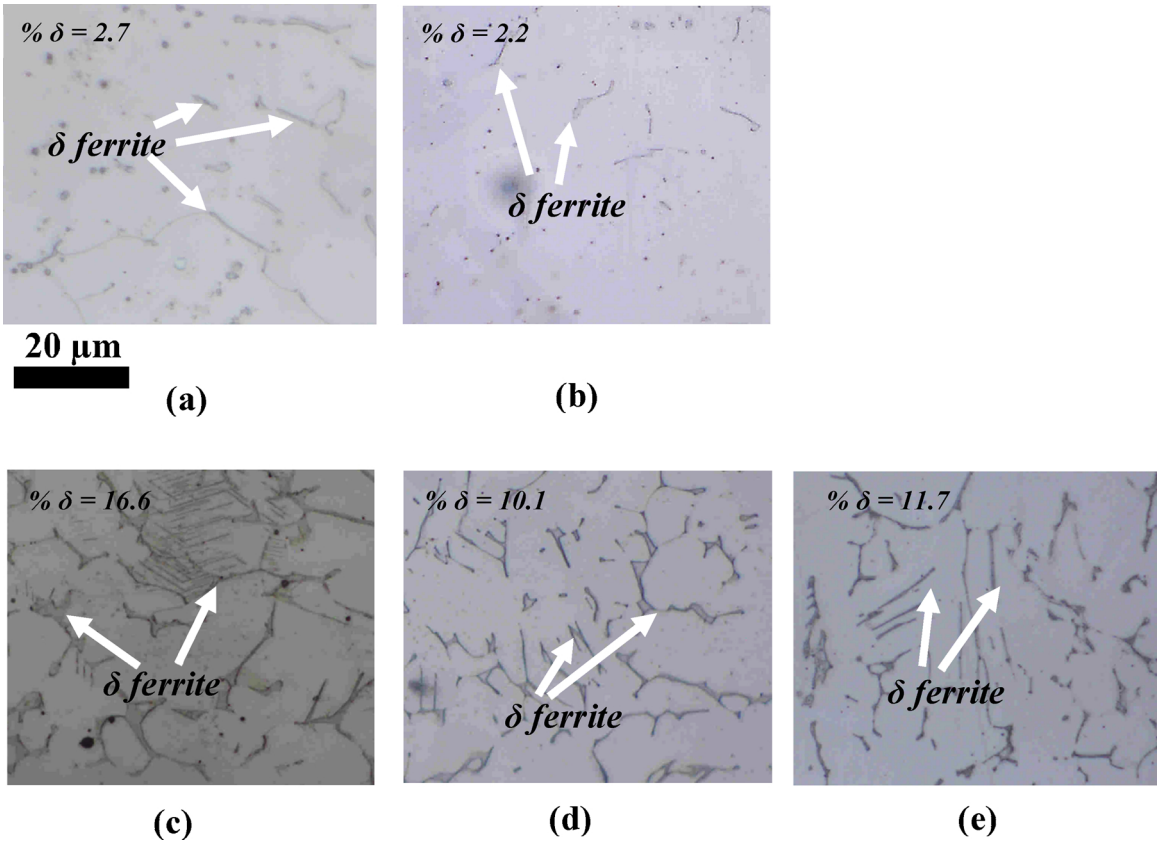

Fig. 4. Optical micrographs of the weld region showing predominantly a skeletal morphology of δ ferrite for (a) sample A, (b) sample B, (c) sample C, (d) sample D and (e) sample E. The selected etching technique could not reveal the grain boundaries of austenite. δ ferrite presence in Sample A and B were practically insignificant. This point was also confirmed through EBSD maps in Fig. 3. The respective ferrite percentages is indicated in the micrographs.

but it is clear from the images that relative amount of phases varied with the heat input. However in the present study no clear trend was observed between the heat inputs and the fraction of δ-ferrite.

More importantly, combinations of welding process variables (different heat inputs) induced significant differences in misorientation and grain boundary fractions of both the phases. This point is illustrated in Fig. 5(a–d). As the objective of the present study was to relate microstructures with processing and mechanical behavior of the joints; it was important to bring out all possible microstructural changes. As can be seen in Fig. 6 a near linear relationship between heat input and grain boundary fractions of γ austenite was observed. This is approximated through lines drawn through the data points. The results indicate that with the increase in the heat input, the cooling rate in the sample decreased and the material remained at higher temperatures for a longer time providing opportunities for grain boundary migration, grain growth driven by the reduction of the grain boundary interfacial energy, and possibly some recrystallization that led to increased fraction of high angle grain boundaries. In those parts of the weld that have undergone significant plastic deformation during cooling, partial recrystallization was expected. This would be expected, for instance, the base metal joint interface that restrained the contraction of the WM. In view of the high heat input and absence of factors inhibiting grain boundary migration, the austenitic grain boundary rapidly migrated and produced very large grains without δ-ferrite precipitation, as seen in Samples A and B. However, under lower heat input, the rate of cooling was increased and the temperature was sufficiently low that any strains that could arise generated fewer dislocations forming sub-structures and that such dislocations were not sufficiently mobile at lower temperature to migrate and annihilate, thus increasing low-angle boundary fractions.

The other important observation concerning the nature of the interface between the austenite and δ-ferrite phases was the possible phase boundary relationship (PBR). These inherent differences between the phases reduce the possibility that the two crystals will match perfectly at the phase interface. As the degree of mismatch between the two adjacent phase lattice increases, the boundary becomes increasingly incoherent, increasing the interfacial strain energy [37]. There are few established relationships most frequently observed in fcc / bcc interfaces which includes Bain, Kurdjumov-Sachs (KS) and Nishyama-Wasserman (NW) relationship. There are also some suggested models (Pitsch and G–T) that is intermediate between KS and NW-orientation relationships (ORs) [38]. Table 3 lists the important ORs that is most observed in fcc/bcc systems that tend to orient the two crystallographically different phases in order to minimize the interfacial energy. The PBR can be defined by specifying an angle and axis of rotation. A quick evaluation in the present study showed dominance of two important PBRs, 44°⟨104⟩ and 44°⟨114⟩. Although 44°⟨104⟩ PBR is deviated through 10–13 ° from ideal Bain relationship, the 44°⟨114⟩ relationship shows large deviations from the standard ORs discussed in Table 3. An attempt has been made to see how close the measured PBRs matches with the established ORs. It is likely that having a crystallographic orientation relationship across the phase boundaries would marginally reduce the boundary energy. For δ-ferrite distributed in the mixed phase microstructures, see sample C, D and E, a discretion of the user is required to identify the two phases and measure the possible PBR between them. This has been attempted manually for approximately 70–75 austenite-δ-ferrite interfaces. The result of this exercise is summarized in Fig. 7. The relative presence of the two PBRs brings out nearly opposite trends.

The results discussed so far were the key microstructural observations from the weld region. In the subsequent section we attempt to bring out microstructural details of the SS-WM and MS-WM interfaces and the respective HAZ.

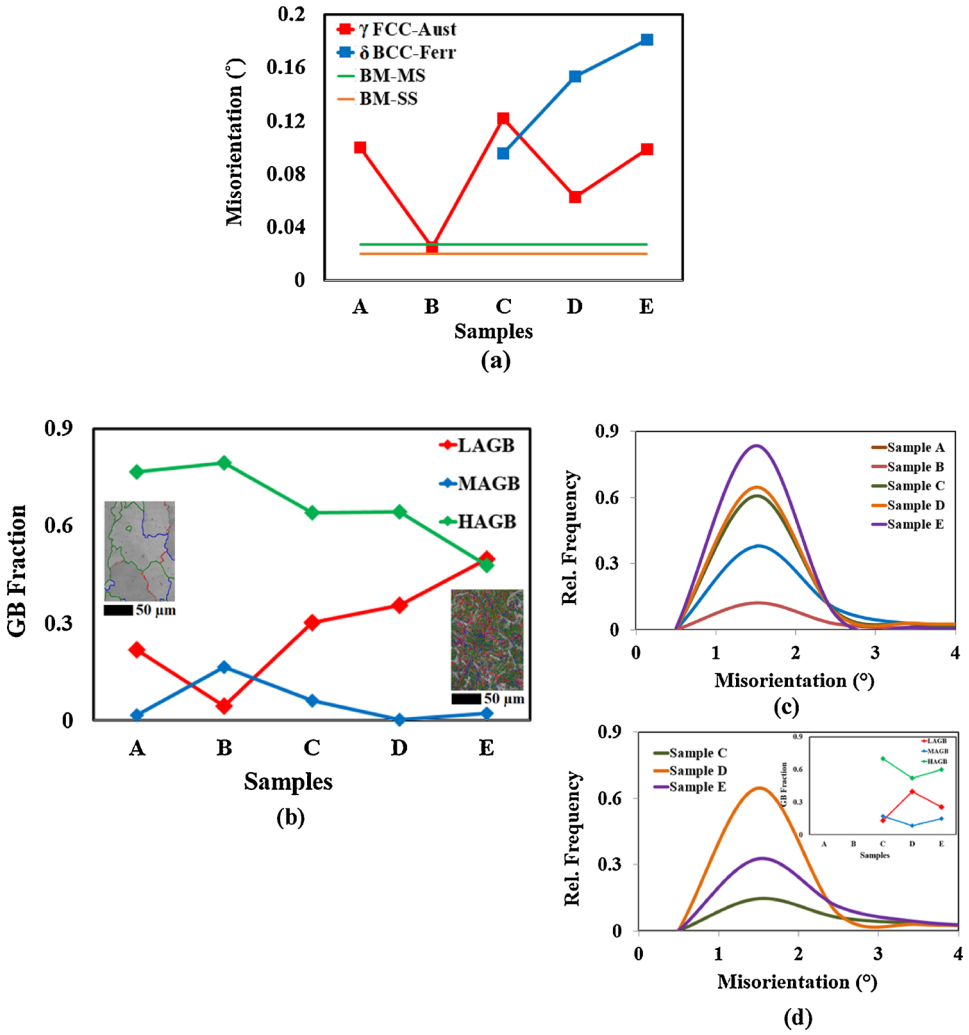

Fig. 5. (a) Average misorientation of both phases in the WM region for all the samples under investigation. (b) γ-fcc grain boundary (GB) fraction plotted for samples A–E. The inset shows image quality (IQ) map superimposed with GB map of the γ-fcc phase. (c), (d) grain boundary distribution of γ-fcc and δ bcc grains respectively. (Color figure online).

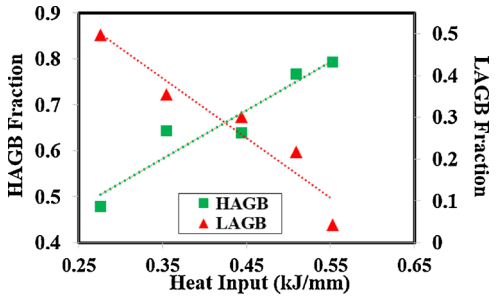

Fig. 6. Grain boundary fractions as a function of heat input. A near linear relationship is observed between grain boundary fractions and heat input. (Color figure online).

Table 3
Summary of known bcc-fcc Orientation Relationships.

OR	Parallel planes and directions	Angle /Axis
Bain	$\{011\}_{BCC}//\{001\}_{FCC}$; $\langle 111\rangle_{BCC}//\langle 110\rangle_{FCC}$	45°/⟨100⟩
K-S	$\{011\}_{BCC}//\{111\}_{FCC}$; $\langle 111\rangle_{BCC}//\langle 110\rangle_{FCC}$	35.3°/⟨110⟩
N-W	$\{011\}_{BCC}//\{111\}_{FCC}$; $\langle 100\rangle_{BCC}//\langle 110\rangle_{FCC}$	45°/⟨110⟩

3.2. Microstructural development at the interfaces and HAZ

In this section, the microstructures of MS-WM and the SS-WM interface are discussed separately. The HAZ and the FZs are labelled through visual approximation. The SS-WM interface were nearly identical for all samples, however large differences were brought for the MS-WM regions. These differences were mainly due to different heat inputs. Also, the width of the fusion zone (FZ) of the MS-WM increased with the increase in the heat input. This point is explained through the phase maps of MS-WM region in Fig. 8(a, b) for samples A and D. The FZ in sample A shows the presence of a prominent unmixed zone with a much higher α -ferrite content. The unmixed zone exists where a small portion of the base metal has totally melted and re-solidified without undergoing filler metal dilution. As indicated on inverse pole figure (IPF) notation in Fig. 8c, these fine ferrite grains had less orientation spread (and misorientation) than adjacent base metal ferrite grains. 20 randomly grains from the FZ were chosen for this analysis. The right side of the FZ shows limited number of coarse δ-ferrite grains. δ-ferrite presence was very less throughout the sample A and B microstructures. Sample E exhibits a much narrower fusion width. It is observed that, close to the FZ, significant δ-ferrite dendritic structures have formed perpendicular to the FZ extending into the WM in the direction of maximum heat flow. At

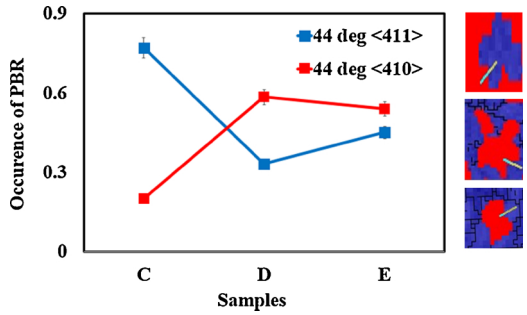

Fig. 7. Number fraction of 44°⟨104⟩ and 44°⟨114⟩ γ austenite—δ-ferrite phase boundaries for samples C, D and E estimated manually for visible γ - δ phase interfaces. The 44°⟨104⟩ boundaries was within 10–13 ° deviation from the ideal Bain relationship. (Color figure online).

lower heat inputs, as in Sample E, the cooling rate was relatively higher, resulting in a sharp change in thermal gradients in the weld metal. This resulted in more dendritic networks of finer size (less time was available for dendrites to grow) [39,40]. At higher heat inputs, the cooling rate was slower, resulting in coarser dendrites, but not a continuous network. The formation of δ-ferrite and the interaction of the base metal grains with the FZ grains occur simultaneously during a welding process and therefore their individual influence on the development of the microstructure is very difficult to isolate.

The microstructures of FZs for the SS—WM region are not very clearly evident. For the sample A, Fig. 9a, the FZ is approximated as the region where a transition of grain morphology from the WM to the BM is observed. This region was still distinct in Sample E, constituting fine δ-ferrite grains in the outlined band shown in Fig. 9b. δ-ferrite presence in the HAZ is visible in certain regions which could be due to local fluctuations in cooling rate. Fig. 10(a, b) explains the misorientation profile of the HAZ and FZ for different samples. The horizontal lines indicate the misorientation value in base metal (BM) microstructures. However, no clear trend in misorientation has been observed with the heat inputs.

3.3. Mechanical properties and its correlation to microstructure

Tensile tests were carried out to evaluate the strength of the joints. All the specimens failed at the weld metal region without any significant necking. The main findings on the tensile strengths of the joints are summarized in Table 4 based on applied heat inputs. The results of tensile tests in Table 4 brings out that the strength and elongation to failure varies in a linear trend.

Of all the different microstructural parameters, the mechanical strength variation is in close correlation with the presence of low angle (dislocation) boundaries, see Fig. 11a. Increase or decrease of UTS matched well with the LAGBs of the γ austenite phase except for sample E. Yield strength does not display any noticeable change though. It is seen that LAGBs form in the grain interior as sub-grain structures or

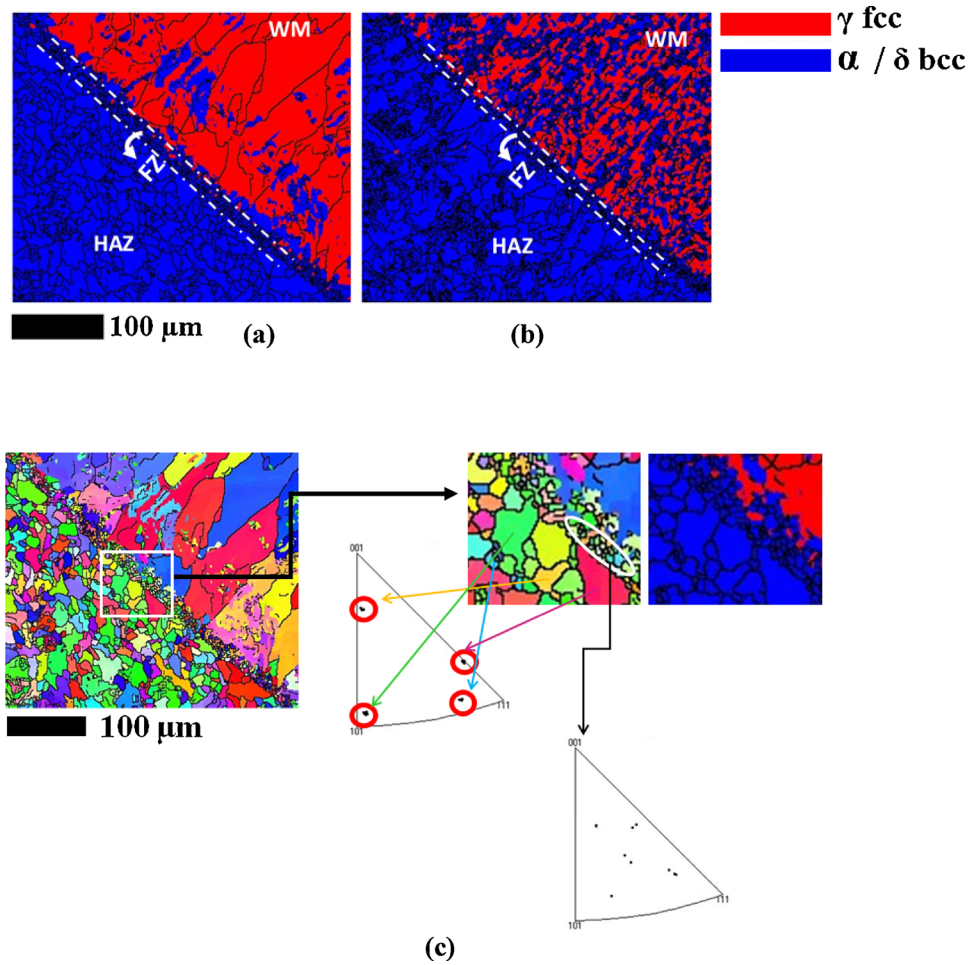

Fig. 8. Phase maps of the MS-WM interface for (a) sample A and (b) sample D. Differences in microstructures are seen in the heat affected zone (HAZ), width of the fusion zone (FZ) and distribution of δ ferrite grains. The FZ is visually approximated by a pair of lines. The δ ferrite grains are seen to grow perpendicular to the FZ. (c) A magnified image of the IPF map of sample A shows large presence of fine grains in the FZ. As indicated in the discrete IPF notation, these fine grains had less orientation spread than the HAZ grains which show relatively wider orientation spread. (Color figure online).

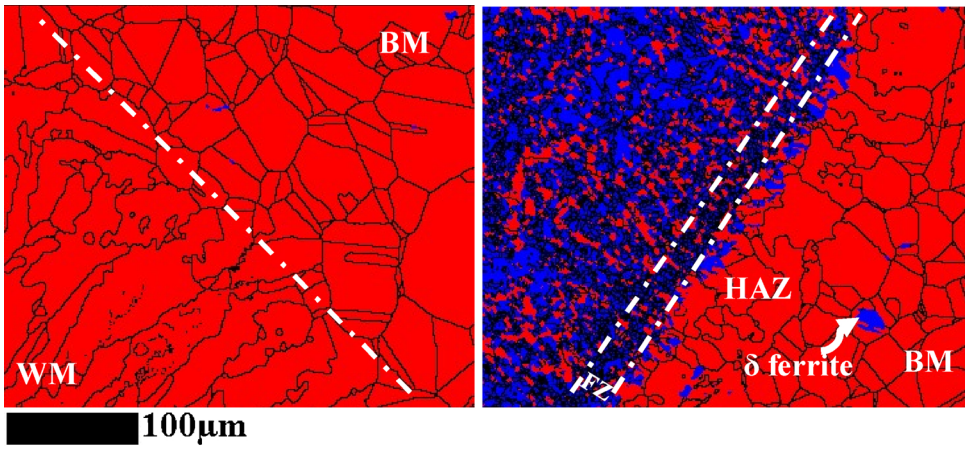

Fig. 9. Phase maps of the SS-WM interface for (a) sample A and (b) sample D. For sample A no clear demarcation between the FZ and WM exists. The FZ has been roughly approximated as the transition region between the WM and BM grains. The SS grains have a polygonal structure with significant twins. The WM grains exhibits an elongated structure with serrated grain boundaries. Sample D showed presence of fine grains of δ ferrite in the FZ. δ ferrite presence was also evident in certain regions of the BM as seen in (b). (Color figure online).

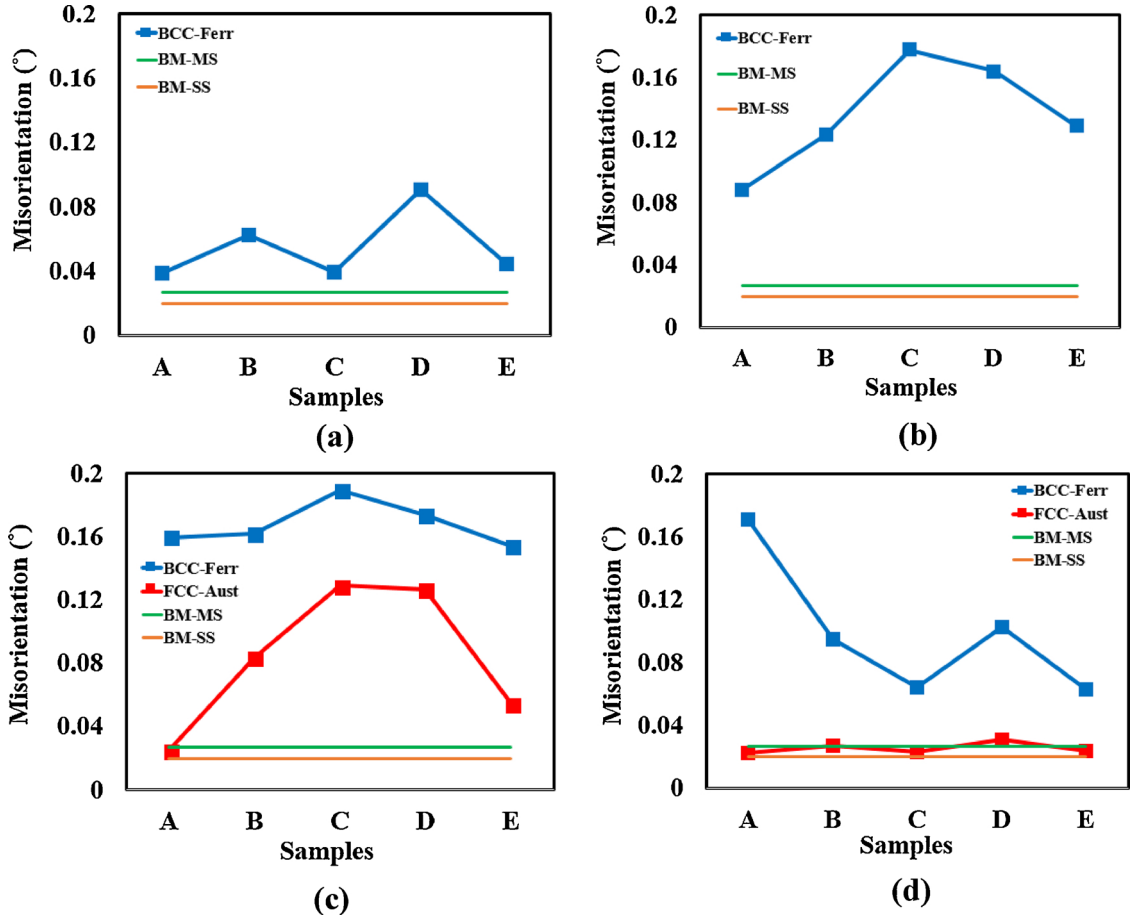

Fig. 10. Effect of sample processing conditions on the local in-grain misorientation in (a) FZ of MS-WM, (b) HAZ of MS-WM, (c) FZ of SS-WM and (d) HAZ of SS-WM. For estimation of misorientation in the FZ, a suitable region was cropped manually for analysis. (Color figure online).

dislocation walls and the driving force for their formation results in the reduction in stored energy in order to maintain some form of structural integrity at the boundary. LAGBs exhibits a discrete dislocation array while HAGBs, in general, maintain a disordered structure. With increase in the LAGB density, these dislocation walls are refined, thereby impeding the movement of slip dislocations (mobile dislocations) across the boundaries leading to strengthening of the weld joint when stress is applied. The increase in ductility with increased strength can be attributed to the movement of LAGB cells as a single unit when subjected to stress. The mobility of the LAGB units depend on the rate at which the dislocations in the boundary can undergo 'climb' [41]. These dislocation walls migrate to the nearest HAGBs where they get locked and the driving force for the mobility of these sub-grain arrays is the stored energy associated to these boundaries. As illustrated in Fig. 11b, the LAGB fraction correlates well with the calculated stored energy from the Read-Shockley equation using EBSD obtained grain boundary misorientation criterion. The decreased strength and ductility of sample E with increase in the LAGB can be related to the lower stored energy that reduced the mobility of these sub-grain dislocations to undergo deformation leading to fracture at lower strength.

Table 4
Obtained ultimate tensile strength (UTS), yield strength (YS) and % elongation to failure values for each material under different heat inputs selected for this study. The mean values of three tensile tests data conducted for each specimen is considered.

Sample	Heat Input (kJ mm^{-1})	UTS (MPa)	YS (MPa)	Elongation (%)
A	0.5093	593	271	24.5
B	0.5524	475	168	12
C	0.4436	536.5	256.	23.4
D	0.3549	573	224	32
E	0.2757	455	244	10.5

The Charpy V-notch (CVN) impact test results for the dissimilar welds are summarized in Table 5. The observed decrease in impact energy of weld metals is attributed to an increase in the local in-grain misorientation of the austenite grains. Fig. 12 a shows that, impact energy decreases with increase in misorientation. Higher local misorientation in austenite grains is a signature of increased density of dislocations and substructures formed in the grains. The increased dislocation density of austenite phase in samples C, D and E is mainly attributed to plastic strain accommodation due to formation of δ-ferrite. High density of dislocations generated within the austenite as a result of strain accommodation reduces the energy absorption capacity of austenite. Another parameter that could contribute to impact energy is the amount of δ-ferrite phase contained in their microstructure. As seen in samples C, D and E exhibiting distinct two-phase microstructure, the impact energy decreases with increase in the ferrite content. Samples A and B however do not folow this trend. Sample D which shows lower ferrite content has a continuous austenite path surrounding ferrite islands, see Fig. 3. The toughness is essentially governed by the facture resistance of the ductile austenite. Sample C in Fig. 3 on the other hand, shows higher percentage of ferrite surrounding the austenite which has a discontinuous distribution in the ferrite matrix. The high strength ferrite imparts lower toughness in sample C. These results discussed from tensile and impact test appear to be the only plausible explanation for microstructural- mechanical behavior relationship.

Table 5
Impact energy (J) measured using Charpy-V notch impact test for all sample conditions.

Sample	Impact Energy (J)
A	113
B	118
C	104
D	117
E	109sss

3.4. Fractogrpahy analysis

The analysis of the fractured cross-section reveals a ductile fracture characterized by the presence of microscopic pits (dimples) and voids of varying size and shapes. The typical fractographic characteristics of tensile fractured surfaces are summarized in the SEM images in Fig. 13 (a–e) under the same magnification.

In Sample A, it is clearly noted that the fractured surface had large planar faceted fracture (shallower pits) where a highly localized shear rupture took place. As a result, the faceted structures were seen to be highly strained. The results also indicated that growth of microvoids primarily occurred in regions of high stress concentration. With further growth of these microvoids, the remaining interconnected links were subjected to shear, leading to unstable crack propagation. On the other hand, the weld samples C and D showed a ductile fracture appearance consisting of equiaxed dimples. Sample D, which had maximum fracture toughness predominantly had microvoids, but a bimodal size distribution was also observed. This gives an indication on the role of

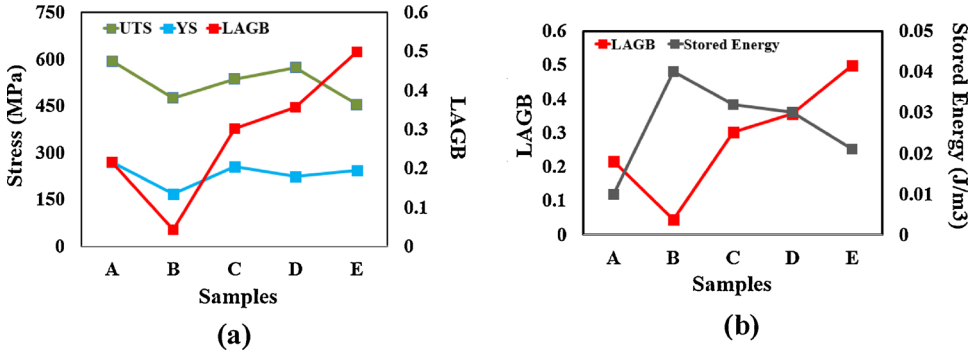

Fig. 11. (a) LAGB fraction plotted with UTS and YS for all the conditions of welded specimens. LAGB fraction correlates with UTS. However sample E shows deviation from this behavior. (b) LAGB fraction and stored energy estimated from Reade-Shockley equation plotted for al samples. Increase in the LAGB fraction corresponds to reduction in stored energy.

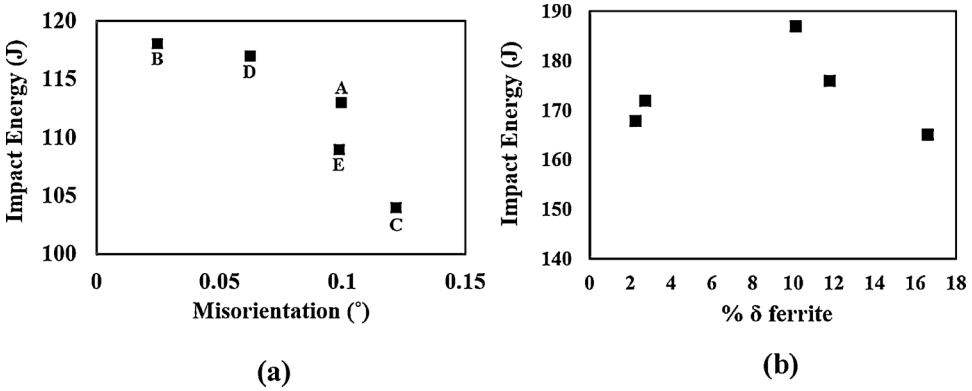

Fig. 12. Impact energy as function of (a) austenite local in-grain misorientation and (b) % δ ferrite. Impact energy is observed to decrease with austenite misorientation and content of δ ferrite in visible two-phase samples.

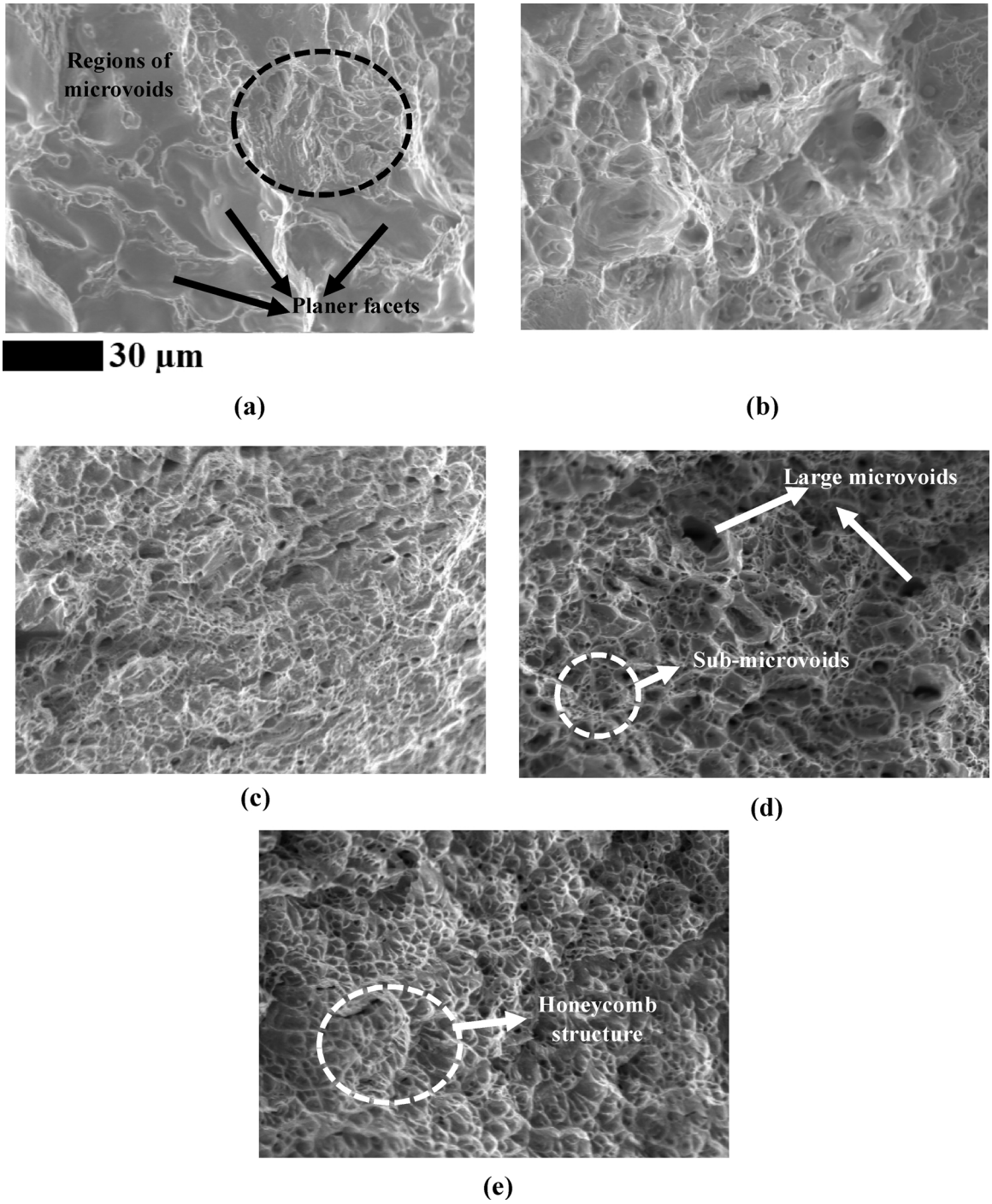

Fig. 13. Fractured features under tensile deformation for (a) sample A, (b) sample B, (c) sample C, (d) sample D and (e) sample E. Though major mode of fracture was ductile, alteration in heat inputs brought out significant differences observed through faceted surfaces, dimple and void distribution.

inclusions (large microvoids) and carbides (sub-microvoids) in the weld fracture process. It is known that carbides require a much higher local deformation, i.e. energy required for nucleation of voids and dimples are higher than required for inclusions. Therefore, it can be concluded that the maximum fracture toughness exhibited by sample D is due to the prevalence of microvoid nucleation around the carbide particles. Sample E had a honeycomb structure that showed protuberances that appear to be "pulled-out"' with no significant dimples and voids. This concerns the low permanent deformation ability of these materials along the axial loading direction requiring a low deformation energy, although it was still in the elasto-plastic range.

The above observation on the fracture modes of the welded samples is at best speculative, but seems to be the only justification to understand the failure mechanism.

4. Conclusions

Five different samples were prepared through dissimilar welding of a stainless steel and a medium carbon steel grade conducted through TIG welding process by varying the conditions of current, voltage and welding speed. These specimens were subjected to tensile deformation. Results on the microstructure development and tensile behavior is briefly summarized.

(1) Significant differences were brought out in the weld microstructure. The microstructures had large elongated grains of single phase γ austenite, serrated grains and also different distribution of δ-ferrite and γ austenite grains of smaller sizes. Differences in microsturtures were also seen through EBSD estimated local misorientation and grain boundary fractions of both phases. The differences observed in the distribution of δ and γ phases in different samples have been related to the heat input and solidification rate of the weld pool.
(2) Investigation on the phase boundary nature between austenite and δ-ferrite in the microstructure revealed dominance of two different PBRs, 44°⟨104⟩ and 44°⟨114⟩. Though PBR of 44°⟨104⟩ deviated from ideal Bain relationship through 10–13 °, 44°⟨114⟩ did not match well with the standard KS NW and Bain orientation relationships (OR). These ORs tend to minimize the interfacial energy at the phase boundaries.
(3) Microstructures of the interfaces MS-WM and SS-WM and their respective HAZs in all these samples varied significantly. The FZ at the MS-WM interface showed presence of very fine grains of α ferrite which were found to be relatively less strained than the neighboring BM ferrite grains. These grains appear as a result of melting and re-solidification of the base metal close to the weld pool without undergoing filler metal dilution. The FZ of SS-WM were not also very different between the different samples. No clear pattern in the local misorientation variation in the HAZ and FZ, between different samples has been observed with the heat inputs.
(4) Correlation of tensile behavior to the microstructure development in the samples revealed that UTS and LAGB fractions followed nearly identical trend. The increased strength corresponds to higher LAGB fractions that results in formation of finely spaced dislocation walls which act as barrier to mobile dislocations. On the other hand it has been postulated that a higher ductility with increased LAGBs results when the dislocation walls undergo a climb motion. The mobility of these LAGBs or the dislocation walls is related to the stored energy associated with the LAGBs.
(5) Impact energy is seen to be a clear function of austenite misorientation. Increased misorientation or dislocation in austenite grains decreases the impact energy. Increase in the ferrite content also reduces the impact energy for samples exhibiting a two-phase microstructure.
(6) Fractured surface reveals that primary mode of fracture was ductile in nature. However, each sample exhibited a uniquely different morphology. This had faceted structures, equiaxed dimples, micro and sub-microvoids, honeycomb structures that gives a fair idea about the pattern of failure in these materials during tensile deformation.

References

[1] Sireesha M, Shankar V, Albert SK, Sundaresan S. Microstructural features of dissimilar welds between 316LN austenitic stainless steel and alloy 800. Mater Sci Eng A 2000;292:74–82. https://doi.org/10.1016/S0921-5093(00)00969-2.
[2] Kuo CH, Tseng KH, Chou CP. Effect of activated TIG flux on performance of dissimilar welds between mild steel and stainless steel. Key Eng Mater 2011;479:74–80. https://doi.org/10.4028/www.scientific.net/KEM.479.74.
[3] Joseph A, Rai SK, Jayakumar T, Murugan N. Evaluation of residual stresses in dissimilar weld joints. Int J Press Vessel Pip 2005;82:700–5. https://doi.org/10.1016/j.ijpvp.2005.03.006.
[4] Arivazhagan N, Singh S, Prakash S, Reddy GM. An assessment of hardness, impact strength, and hot corrosion behaviour of friction-welded dissimilar weldments between AISI 4140 and AISI 304. Int J Adv Manuf Technol 2008;39:679–89. https://doi.org/10.1007/s00170-007-1266-7.
[5] Kotecki DJ, Lippold JC. Welding metallurgy and weldability of stainless steels. Hoboken, New Jersey: John Wiley; 2005. https://doi.org/10.1002/9781118960332.
[6] Jafarzadegan M, Feng AH, Abdollah-Zadeh A, Saeid T, Shen J, Assadi H. Microstructural characterization in dissimilar friction stir welding between 304 stainless steel and st37 steel. Mater Charact 2012;74:28–41. https://doi.org/10.1016/j.matchar.2012.09.004.
[7] Derazkola HA, Aval HJ, Elyasi M. Analysis of process parameters effects on dissimilar friction stir welding of AA1100 and A441 AISI steel. Sci Technol Weld Join 2015;20:553–62. https://doi.org/10.1179/1362171815Y.0000000038.
[8] Sharma G, Dwivedi DK. Study on microstructure and mechanical properties of dissimilar steel joint developed using friction stir welding. Int J Adv Manuf Technol 2017;88:1299–307. https://doi.org/10.1007/s00170-016-8763-5.
[9] Logan BP, Toumpis AI, Galloway AM, McPherson NA, Hambling SJ. Dissimilar friction stir welding of duplex stainless steel to low alloy structural steel. Sci Technol Weld Join 2016;21:11–9. https://doi.org/10.1179/1362171815Y.0000000063.
[10] Buzolin RH, Francisco BR, da Silva EP, Pereira VF, Ramirez Londono AJ, Maluf O, et al. Dissimilar friction stir welding of HSLA steel to austenitic High-Mn TRIP steel. Mater Sci Forum 2016;879:2306–11. https://doi.org/10.4028/www.scientific.net/MSF.879.2306.
[11] Sadeghian M, Shamanian M, Shafyei A. Effect of heat input on microstructure and mechanical properties of dissimilar joints between super duplex stainless steel and high strength low alloy steel. Mater Des 2014;60:678–84. https://doi.org/10.1016/j.matdes.2014.03.057.
[12] Hajiannia I, Shamanian M, Kasiri M. Microstructure and mechanical properties of AISI 347 stainless steel/A335 low alloy steel dissimilar joint produced by gas tungsten arc welding. Mater Des 2013;50:566–73. https://doi.org/10.1016/j.matdes.2013.03.029.
[13] Cam G, Yeni C, Erim S, Ventzke V, Kocak M. Investigation into properties of laser welded similar and dissimilar steel joints. Sci Technol Weld Joint 1998;3(4):177–89.
[14] Rossini M, Spena PR, Cortese L, Matteis P, Firrao D. Investigation on dissimilar laser welding of advanced high strength steel sheets for the automotive industry. Mater Sci Eng A 2015;628:288–96. https://doi.org/10.1016/j.msea.2015.01.037.
[15] Hernandez BVH, Kuntz ML, Khan MI, Zhou Y. Influence of microstructure and weld size on the mechanical behaviour of dissimilar AHSS resistance spot welds. Sci Technol Weld Join 2008;13:769–76. https://doi.org/10.1179/136217108X325470.
[16] Pouranvari M, Mousavizadeh SM, Marashi SPH, Goodarzi M, Ghorbani M. Influence of fusion zone size and failure mode on mechanical performance of dissimilar resistance spot welds of AISI 1008 low carbon steel and DP600 advanced high strength steel. Mater Des 2011;32:1390–8. https://doi.org/10.1016/j.matdes.2010.09.010.
[17] Mújica Roncery L, Weber S, Theisen W. Welding of twinning-induced plasticity steels. Scr Mater 2012;66:997–1001. https://doi.org/10.1016/j.scriptamat.2011.11.041.
[18] Mittal R, Sidhu BS. Microstructures and mechanical properties of dissimilar T91/347H steel weldments. J Mater Process Technol 2015;220:76–86. https://doi.org/10.1016/j.jmatprotec.2015.01.008.
[19] Devendranath Ramkumar K, Singh A, Raghuvanshi S, Bajpai A, Solanki T, Arivarasu M, et al. Metallurgical and mechanical characterization of dissimilar welds of austenitic stainless steel and super-duplex stainless steel – a comparative study. J Manuf Process 2015;19:212–32. https://doi.org/10.1016/j.jmapro.2015.04.005.
[20] Vashishtha H, Taiwade RV, Sharma S, Patil AP. Effect of welding processes on microstructural and mechanical properties of dissimilar weldments between conventional austenitic and high nitrogen austenitic stainless steels. J Manuf Process 2017;25:49–59. https://doi.org/10.1016/j.jmapro.2016.10.008.
[21] Lundin CD. Dissimilar metal welds-transition joints literature review. Weld J 1982;61:58s.
[22] Mvola B, Kah P, Martikainen J. Dissimilar ferrous metal welding using advanced gas metal arc welding processes. Rev Adv Mater Sci 2014;38:125.
[23] Pouraliakbar H, Hamedi M, Kokabi AH, Nazari A. Designing of CK45 carbon steel and AISI 304 stainless steel dissimilar welds. Mater Res 2014;17:106–14. https://doi.org/10.1590/S1516-14392013005000170.
[24] Klueh RLKJF. Austenitic stainless steel-ferritic steel weld joint failures. Weld J 1982:302–11.
[25] Hou J, Peng Q, Xue H, Takeda Y, Kuniya J, et al. Microstructure and stress corrosion cracking of the fusion boundary region in an alloy 182-A533B low alloy steel dissimilar weld joint. Corros Sci 2010;52:3949–54. https://doi.org/10.1016/j.corsci.2010.08.002.
[26] Hou J, Peng QJ, Takeda Y, Kuniya J, Shoji T, Wang JQ, et al. Microstructure and mechanical property of the fusion boundary region in an alloy 182-low alloy steel dissimilar weld joint. J Mater Sci 2010;45:5332–8. https://doi.org/10.1007/s10853-010-4581-6.
[27] Cao J, Gong Y, Zhu K, Yang ZG, Luo XM, Gu FM. Microstructure and mechanical properties of dissimilar materials joints between T92 martensitic and S304H austenitic steels. Mater Des 2011;32:2763–70. https://doi.org/10.1016/j.matdes.2011.01.008.
[28] Mujica L, Weber S, Pinto H, Thomy C, Vollertsen F. Microstructure and mechanical properties of laser-welded joints of TWIP and TRIP steels. Mater Sci Eng A 2010;527:2071–8. https://doi.org/10.1016/j.msea.2009.11.050.
[29] Ranjbarnodeh E, Hanke S, Weiss S, Fischer A. Effect of welding parameters on the heat-affected zone of AISI409 ferritic stainless steel. Int J Miner Metall Mater 2012;19:923–9. https://doi.org/10.1007/s12613-012-0648-5.
[30] Badheka VJ, Basu R, Omale J, Szpunar J. Microstructural aspects of TIG and A-TIG welding process of dissimilar steel grades and correlation to mechanical behavior. Trans Indian Inst Met 2016:69. https://doi.org/10.1007/s12666-016-0836-5.
[31] Cao WQ, Gu CF, Pereloma EV, Davies CHJ. Stored energy, vacancies and thermal stability of ultra-fine grained copper. Mater Sci Eng A 2008;492:74–9. https://doi.org/10.1016/j.msea.2008.02.048.
[32] Rodriguez-Ibabe JM, López B. Thermomechanical processing and role of microalloying in eutectoid steels. In: Weng Y, Dong H, Gan Y, editors. Advanced steels. Heidelberg: Springer; 2011. p. 475–84.
[33] Suutala N, Takalo T, Moisio T. The relationship between solidification and microstructure in austenitic and austenitic-ferritic stainless steel welds. Metall Trans A

1979;10:512–4. https://doi.org/10.1007/BF02697081.
[34] Brooks JA, Thompson AW. Microstructural development and solidification cracking susceptibility of austenitic stainless steel welds. Int Mater Rev 1991;6:1644.
[35] Hunter A, Ferry M. Phase formation during solidification of AISI 304 austenitic stainless steel. Scr Mater 2002;46:253–8.
[36] Zhang XF, Terasaki H, Komizo Y. Correlation of δ-ferrite precipitation with austenite grain growth during annealing of steels. Philos Mag Lett 2011;91:491–7. https://doi.org/10.1080/09500839.2011.587464.
[37] Nelson TW, Lippold JC, Mills MJ. Nature and evolution of the fusion boundary in ferritic-austenitic dissimilar weld metals, Part 1 - nucleation and growth. Weld J 1999;78:329–37.
[38] He Y, Godet S, Jonas JJ. Observations of the Gibeon meteorite and the inverse Greninger-Troiano orientation relationship. J Appl Crystallogr 2006;39:72–81. https://doi.org/10.1107/S0021889805038276.
[39] Kumar S, Shahi AS. Effect of heat input on the microstructure and mechanical properties of gas tungsten arc welded AISI 304 stainless steel joints. Mater Des 2011;32:3617–23. https://doi.org/10.1016/j.matdes.2011.02.017.
[40] Jana S. Effect of heat input on the HAZ properties of two duplex stainless steels. J Mater Process Technol 1992;33:247–61. https://doi.org/10.1016/0924-0136(92)90211-A.
[41] Rollett AD, Gottstein G, Shvindlerman LS, Molodov DA. Grain boundary mobility – a brief review. Zeitschrift Für Met 2004;95:226–9. https://doi.org/10.3139/146.017938.